Imaging Periodic Currents Using Alternating Balanced Steady-State Free Precession

Giedrius T. Buračas,* Thomas T. Liu, Richard B. Buxton, Lawrence R. Frank, and Eric C. Wong

Existing functional brain MR imaging methods detect neuronal activity only indirectly via a surrogate signal such as deoxyhemoglobin concentration in the vascular bed of cerebral parenchyma. It has been recently proposed that neuronal currents may be measurable directly using MRI (ncMRI). However, limited success has been reported in neuronal current detection studies that used standard gradient or spin echo pulse sequences. The balanced steady-state free precession (bSSFP) pulse sequence is unique in that it can afford the highest known SNR efficiency and is exquisitely sensitive to perturbations in free precession phase. It is reported herein that when a spin phase-perturbing periodic current is locked to an RF pulse train, phase perturbations are accumulated across multiple RF excitations and the spin magnetization reaches an alternating balanced steady state (ABSS) that effectively amplifies the phase perturbations due to the current. The alternation of the ABSS signal therefore is highly sensitive to weak periodic currents. Current phantom experiments employing ABSS imaging resulted in detection of magnetic field variations as small as 0.15nT in scans lasting for 36 sec, which is more sensitive than using gradient-recalled echo imaging. Magn Reson Med 59: 140–148, 2008. © 2007 Wiley-Liss, Inc.

Key words: balanced SSFP; alternating balanced steady state; neuronal currents; oscillating equilibrium

Since discovery of the blood oxygenation level-dependent (BOLD) effect by Ogawa et al. (1), MRI has become a dominant tool for mapping brain function. Despite the spectacular success of BOLD imaging due to its noninvasive nature and unprecedented uniformly high spatial resolution, this method remains complementary to more traditional techniques such as electroencephalography (EEG) and magnetoencephalography (MEG) that afford high temporal resolution and tap directly into electrical activity generated by neuronal populations of cerebral parenchyma. However, MEG and EEG measures of neuronal population activity are affected by massive superposition of fields due to many current dipoles. In addition, EEG is susceptible to spatiotemporal filtering by various tissues. These factors degrade spatial resolution substantially and make it difficult to image deep structures.

Is there a way to combine the direct nature of EEG/MEG measurements with the high spatial resolution of MRI? Recent studies of the feasibility of measuring magnetic fields induced by neuronal currents by means of MRI (ncMRI) give hope that these limitations can be overcome. At the location of MEG detector SQUIDs, removed from cortical current dipole sources by >20–40 mm, the evoked magnetic field reaches $\Delta B = 10^{-12}$ T = 1 pT (e.g., 2). Indeed, since the magnetic field associated with current dipoles is expected to fall off as the inverse square of distance, calculations of the peak magnetic field strength in voxels (acquired using MRI) adjacent to such current dipoles yield $\Delta B = 0.1$ nT for evoked responses, and ≈1 nT for spontaneous rhythms (3,4). Studies using current (3,5–8), current dipole (4), and columnar current (9) phantoms have achieved sensitivity in the range of 0.1–1 nT, which is on the order of that necessary to detect neuronal currents. Detection of spontaneous neuronal activity in vitro has been reported (10). Recent in vivo ncMRI studies have addressed neuronal currents associated with epileptic seizures (11) and normal spontaneous α-rhythm activity (12,13). Neuronal currents in cerebral cortex evoked in response to sensorimotor activity (14–16) and in the optical nerve evoked by strobe stimulation (7,8) have also been reported. However, the observability of the spontaneous alpha-wave activation in cortex (13,14) and the evoked ncMRI signal in cortex remains a matter of debate (e.g., 16–18). Indeed, ncMRI based on standard gradient and spin echo pulse sequences to date has not yielded a robust method that would afford reliable detection of the neuronal currents in cerebral cortex.

We propose that the key limitation of the neural current detection methods used heretofore is relatively low SNR due in part to the phase perturbation integration time $\Delta\tau$, which in gradient and spin echo experiments is limited by TE. This limitation can be overcome by employing balanced steady-state free precession pulse sequences (bSSFP; also known as FIESTA, True FISP, Balanced FFE; see Ref. 19), that are known to induce magnetization steady states highly sensitive to phase offsets. Balanced SSFP pulse sequences are unique in that they can afford the highest known SNR per unit time (20). Because of its very high SNR efficiency and speed, bSSFP imaging is becoming increasingly popular due to recent availability of high-performance gradients. Recently, bSSFP pulse sequences have been applied for cardiac cine imaging (21), MR elastography (22), and angiography (23). Thus, application of bSSFP for functional neural current imaging can potentially solve the problem of low SNR.

Moreover, recent studies suggest that SSFP sequences can be exquisitely sensitive to minute periodic perturbations in the free precession phase between RF pulses, as long as the RF excitation is synchronized to the periodic perturbations (22,23). Herein we study alternating balanced steady states (ABSS) of a spin isochromat induced

Department of Radiology, UCSD Center for Functional MRI, La Jolla, California.

*Correspondence to: Giedrius Buracas, UCSD Center for Functional MRI, Keck Bldg., MC 0677, 9500 Gilman Dr., La Jolla, CA 92037. E-mail: gburacas@ucsd.edu

Received 8 May 2007; revised 26 September 2007; accepted 1 October 2007.
DOI 10.1002/mrm.21457
Published online 29 November 2007 in Wiley InterScience (www.interscience.wiley.com).

by periodic electric currents locked to RF excitation pulses (see Fig. 1a). Such alternating steady states accumulate phase perturbations across many repeats (TRs) and effectively amplify the phase offset induced by currents. We demonstrate a high sensitivity of bSSFP-based imaging methods to periodic currents. Our data acquired with bSSFP at 3T using a current phantom is shown to achieve an SNR sufficient to detect signal induced by periodic neuronal currents. We conclude that application of bSSFP for ncMRI has a potential of introducing a new MR imaging modality for functional brain imaging: in situ MEG that affords high spatial resolution.

THEORY

Direct Imaging of Neuronal Currents Using MRI

MR imaging of electric currents rests on the fact that a current dipole perpendicular to the scanner main magnetic field B_0 creates a magnetic field component ΔB_z parallel to B_0, which perturbs the phase ϕ of precessing ^{1}H spins in proportion to the current magnitude and duration $\Delta\tau$: $\Delta\phi = 2\pi\gamma\Delta B_z\Delta\tau$, where γ is the ^{1}H gyromagnetic ratio. For example, a perturbation of $\approx$1nT lasting for 30 ms will result in phase accrual of $\approx$0.5°. The resulting perturbation in B_0 may also affect the dephasing of precessing ^{1}H spins in a voxel. Then the net phase variation can be registered in a phase image, and spin dephasing can be registered in a standard magnitude image. All ncMRI studies to date have employed either gradient or spin-echo pulse sequences in which the field modulation is detected through the phase modulation accrued during a single TE period (but see Ref. 6).

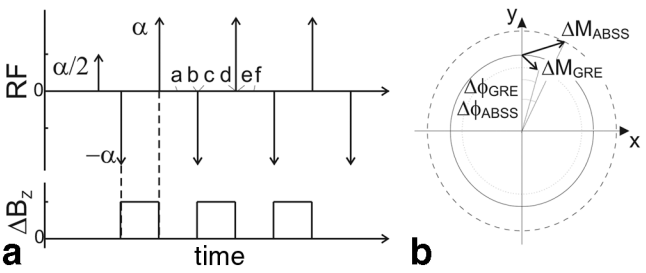

FIG. 1. The conceptual basis of the ABSS method for imaging neural currents and its comparison to GRE imaging. **a**, Top: Initial eight RF pulses of the bSSFP pulse sequence. The sequence starts with a catalytic RF pulse of angle $\alpha/2$ and the first repetition interval of TR/2 ms, then alternates the sign of the RF pulse (180° phase cycling). Bottom: The time-course of the applied RF-locked current pulses. The current-induced perturbation of magnetic field alternates according to the pattern [ΔB_z, 0, ΔB_z, 0,…], and models alternating activation of a neuronal population. A full period of RF excitation and current perturbation is played out between time points **a** and **f** (see Appendix). **b:** Comparison of the current-modulated MR signal in GRE and ABSS experiments. In a GRE experiment (using a current phantom employed in the present study) the current-induced perturbation of the magnetic field ΔB_z has the greatest impact on the signal phase and a lesser effect on the signal magnitude attenuation due to spin dephasing. In an ABSS experiment both phase and magnitude are affected substantially, and the direction of the effect depends on the static off-resonance. A natural method of comparison of the two signals is to use the magnitude of the modulation of the complex signal (indicated by the arrows).

In a gradient-recalled echo (GRE) experiment the magnetic field generated by neuronal currents potentially can cause changes in both MR signal phase ϕ and magnitude S. Assuming homogenous spin density and a constant ΔB_z for the entire duration TE, but inhomogeneous magnetic field perturbation $\Delta B_z(r)$ within a voxel (here r stands for a position vector), the mean phase accumulation within a voxel at the time TE is $\Delta\phi_v = \langle\Delta\phi(r)\rangle = 2\pi\gamma TE\langle\Delta B_z(r)\rangle$ (12). Here $\langle.\rangle$ denotes the average across a voxel. Field inhomogeneity also results in signal loss due to dephasing, and for small $\Delta\phi$ is given by: $S_v = S_0\,[1 - \langle\Delta\phi(r)^2\rangle/2 + \langle\Delta\phi(r)\rangle^2/2]$ (12). Thus, for a voxel with homogenous ΔB, $\Delta\phi_v$ is linearly proportional to ΔB_z but $S_v = S_0$. By contrast, for a voxel with inhomogeneous ΔB and $\langle\Delta\phi(r)\rangle = 0$ (e.g., the current dipole is in the middle of the voxel and positive and negative contributions cancel each other), the signal is proportional to the variance: $\Delta S_v \propto \langle\Delta\phi(r)^2\rangle$. Figure 1b illustrates that the impact of the current-induced ΔB_z on both the signal magnitude and phase rotation can be succinctly captured by measuring the magnitude of the change in the complex MR signal (24). Note that while the change in GRE signal magnitude is a result of spin dephasing alone, the bSSFP signal magnitude is affected by both spin dephasing and phase rotation and is a function of a static off-resonance frequency.

The contrast-to-noise ratio (CNR) for the induced phase signal can be derived from the fact that the thermal phase noise is inversely proportional to the magnitude SNR: $CNR_\phi = \langle\Delta\phi\rangle S_0/\sigma$, where $SNR = S_0/\sigma$ and σ is standard deviation due to the thermal noise (25). Similarly, the CNR for the induced magnitude signal is: $CNR_{mag} = [\langle\Delta\phi^2\rangle - \langle\Delta\phi\rangle^2]S_0/2\sigma$ (12). Konn et al. (12) conclude that for the biologically realistic distribution of current dipoles and ΔB_z range CNR is dominated by the phase rotation and the contribution from spin dephasing is negligible. Then a simple agar phantom with an insulated wire threaded through the center of the phantom (see Materials and Methods) is a good model for studying the MR effects of minute phase rotation: In voxels that are distant from the current-carrying wire $\langle\Delta B_z\rangle \gg \mathrm{stdev}(\Delta B_z)$, and the voxel-wise homogenous ΔB_z can be assumed. Therefore, a GRE (or spin echo) experiment, assuming no tangible change in signal magnitude, the mean phase rotation $\Delta\phi = 0.5°$ induced in the voxel by a $\Delta B_z \approx$1nT applied for 30 ms leads to a change in the magnitude of the complex signal $\Delta S/S = 100\% \mid 1 - \exp(\Delta\phi\pi j/180) \mid \approx 0.9\%$ (here $j = \sqrt{-1}$, and $\mid . \mid$ is the magnitude of a complex number; see Fig. 1b).

Alternating Balanced SSFP

Balanced SSFP offers greater sensitivity than GRE-based ncMRI. First, the magnitude of the bSSFP signal may exceed that of GRE. At zero resonance offset, given ±180° phase cycling, the bSSFP signal magnitude is proportional to:

$$M_{SS} = M_0\, e_2 \sin(\alpha)(1-E_1)/[1-(E_1-E_2)\cos(\alpha) - E_1E_2], \quad [1]$$

where α is the flip angle, $E_1 = \exp(-TR/T_1)$, $E_2 = \exp(-TR/T_2)$, $e_2 = \exp(-TE/T_2)$, and M_{SS} is transverse magnetiza-

tion (26). Note that the signal decay at the time TE is modeled by e_2 (27,28). In the simulations we used T_1 = 1300 ms and T_2 = 110 ms that match those for the gray matter at 3T (29). The optimal flip angle for bSSFP that generates maximum signal magnitude is given by $\cos(\alpha_{SS}) = (T_1/T_2 - 1)/(T_1/T_2 + 1)$.

By contrast, the signal for a standard GRE sequence is proportional to:

$$M_{GRE} = M_0\, e_2{}^* \sin(\alpha)(1-E_1)/[1-E_1\cos(\alpha)]. \quad [2]$$

where $e_2{}^* = \exp(-TE/T_2{}^*)$. The optimal flip angle is given by the Ernst angle: $\cos(\alpha_{GRE})=E_1$. We used gray matter $T_2{}^*$ = 45 ms (29). Thus, the GRE signal decays faster than the bSSFP signal.

Since the ABSS pulse sequence accumulates phase perturbations over multiple TRs, the modulation due to alternating currents is relatively insensitive to TE. The modulation of GRE signal by currents, by contrast, is linearly related to TE. Therefore, in simulations and experiments we used several TE values (i.e., TE = 3 ms and TE = TR −3 ms, so that TE ≤27 ms). Figure 2a plots bSSFP and GRE signal magnitudes for TR = {10, 30, 50} ms with TE = 7 ms for TR = 10, and TE = 27 ms for TR = {30, 50}. The ratio M_{SS}/M_{GRE} (Fig. 2b) reveals that the bSSFP advantage grows with flip angle, and is maximal for short TR. For example, at the optimal flip angle α_{SS} bSSFP signal exceeds that of GRE by a factor of >3.

Second, in addition to the intrinsic SNR advantage, a greater signal modulation may be achieved with bSSFP as compared to GRE when an ABSS is induced using current that alternates with every RF. During a bSSFP experiment the spin ensemble possessing transverse magnetization precesses between RF pulses by a constant angle determined by off-resonance caused by various physical mechanisms such as B_0 inhomogeneity, phase cycling of the RF pulse, and application of extrinsic factors, including motion-sensitizing gradients and current pulses. If the precession angle is controlled externally so that it alternates with every other TR, an oscillating dynamical equilibrium is reached such that the steady-state signal alternates between two states with every TR. This can be achieved using a periodic alternating current locked to RF pulses (Fig. 1a).

The magnetization vector of a spin isochromat for the two alternating steady states can be expressed in closed form as:

$$M_{SS1} = (1 - A_1)^{-1}B_1, \quad [3]$$

$$M_{SS2} = (1 - A_2)^{-1}B_2,$$

where A_i and B_i are matrices describing spin evolution over a period of alternation (see Appendix for the derivation and Ref. 27).

Figure 3 shows transverse magnetization magnitudes (relative to initial magnetization M_0) and phases for the two alternating steady states as a function of static off-resonance $\Delta\phi$ for RF-locked alternating current that induces phase rotation alternating between $\delta\phi_1 = 0$ and $\delta\phi_2 = 0.5°$. Sequence timing parameters were T_1/T_2/TR/TE= 1000/80/30/27 ms, tip angle 27°, and the magnetization M_{xy} was calculated at the echo time. The magnitude profiles of the two steady states exhibit mirror symmetry across the 0 off-resonance line (see Fig. 4b; Ref. 22).

At steady state induced by the bSSFP sequence the phase of a spin isochromat with a transverse magnetization component is affected by off-resonance throughout the repetition time TR. Thus, a ΔB_z perturbation induced by a current pulse between two excitation pulses contributes to the steady state phase throughout TR, in contrast to a GRE sequence that can accumulate the phase perturbation only for the time TE. Thus, when calculating the sensitivity of the ABSS imaging to currents we can use the following expression: $\delta\phi = 2\pi\gamma\Delta B_z TR$. For TR = 30 ms, a 0.5° phase offset is created by a perturbation $\Delta B_z \approx 1.1$nT. Figure 4 illustrates ABSS signal modulation as a function

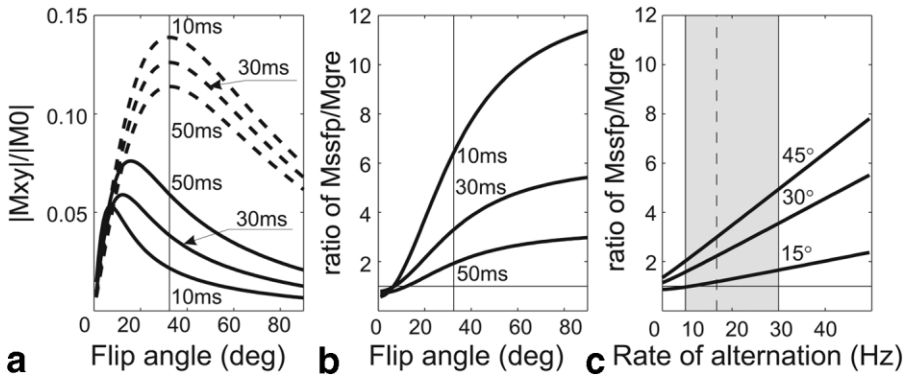

FIG. 2. GRE vs. bSSFP signal as a function of flip angle and TR. **a:** GRE (continuous line) and bSSFP (broken line) transverse magnetization (relative to M_0) as a function of the flip angle plotted for three TR values (TR/TE = 10/7 ms, 30/27 ms, and 50/27 ms). The relaxation parameters are assumed to be: T_1 = 1300 ms, T_2 = 110 ms; $T_2{}^*$ = 45 ms). The optimum flip angle for bSSFP is ≈30° regardless of the TR, while the Ernst angle (≈10°) depends on TR. **b:** The ratio of bSSFP/GRE magnetization (as in **a**) as a function of flip angle plotted for TR/TE = 10/7 ms, 30/27 ms, and 50/27 ms. The maximum bSSFP advantage is achieved for short TR and large flip angles. **c:** The ratio of bSSFP/GRE magnetization immediately after the RF pulse as a function of the rate of current alternation (1/2TR). The range of rates applicable for neural current imaging (10–30 Hz) is limited by T_2 and the maximum rate at which neuronal populations may be entrained to stimuli (shaded region).

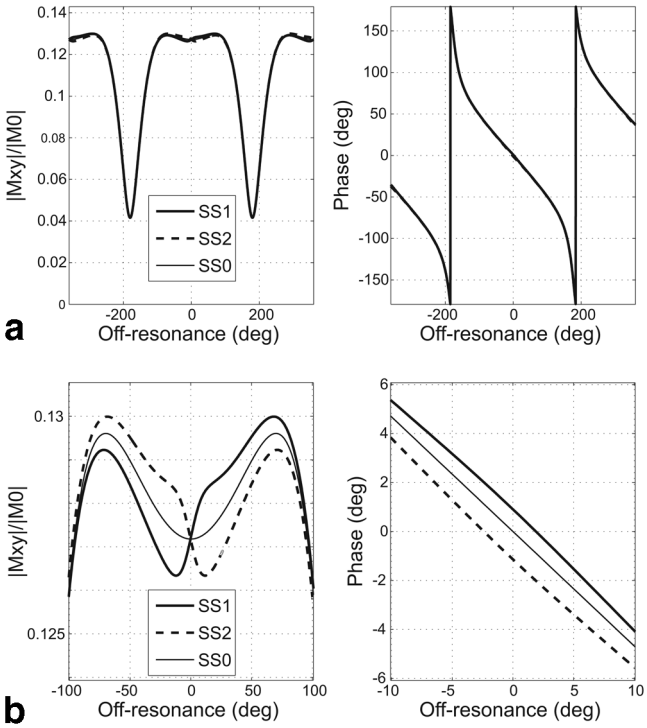

FIG. 3. The magnitude (left column) and the phase (right column) profiles of the transverse magnetization (relative to M_0) in the ABSS experiment as a function of static off-resonance $\phi = 2\pi\phi TR + \delta\phi_i$ for the two alternating steady states corresponding to $\delta\phi_1 = 0.5°$ and $\delta\phi_2 = 0°$. **a:** Continuous and broken lines correspond to the two steady states SS1 (0.5°) and SS2 (0°). **b:** The same off-resonance functions plotted on a finer scale. The magnitude (left) profile is mirror-symmetric around the line at zero off-resonance. The thin line shows the nonoscillating steady state SS0 in the absence of periodic currents. The simulation parameters are T_1/T_2/TR/TE = 1300/110/30/27 ms, flip angle = 27°.

of off-resonance for the set of parameters used for Fig. 3. While amplitude modulation is quite modest and barely exceeds 1.5% (Fig. 4a), complex signal detection results in a maximum modulation of 3.5% at the 0 off resonance (Fig. 4b, continuous black line: TE = 27 ms; broken line: TE = 3 ms). The complex modulation between the two steady states by more than 3% occurs over a rather narrow window of off-resonances centered on zero off-resonance. Contribution of the phase difference and not magnitude difference for the two steady states dominates around zero off-resonance (Fig. 4c, continuous black line: TE = 27 ms; broken line: TE = 3 ms). Thus, the critical property of the dual-equilibrium state is that it can effectively amplify minute differences in precession angle during two consecutive TRs. For the data in Fig. 4c the amplification factor is ≈4 since the phase perturbation of 0.5° is converted around zero off-resonance to the 2° phase deviation. For small precession perturbation angles (≪1°) the gain factor is proportional to T_2/TR and can afford up to 18-fold amplification of phase perturbation (22).

Thus, within an off-resonance interval around zero off-resonance, the ABSS signal modulation by the 1nT periodic pulse lasting for 30 ms is larger than that produced by the GRE ncMRI (0.9%, see above) by a factor of >3. An additional gain in CNR can be expected from the fact that the SNR of the bSSFP signal exceeds that of a GRE signal (Fig. 2).

Temporal Requirements for ncMRI

The electric current imaging method using ABSS requires a rapidly alternating current. On one hand, the lower bound for the alternation rate is determined by T_2 since alternating balanced states can be produced provided that TR < T_2,T_1. At 3T the gray matter T_2 ~98–132 ms (29). Assuming the alternating current is locked to the RF pulses as in Fig. 1a and T_2 > TR = 50 ms, the lower bound for the alternation frequency is ≈10 Hz.

On the other hand, when applying ABSS for neural current imaging the upper bound for this method is given by the maximum frequency at which cerebral neuronal networks can be entrained by a presented external stimulus. Rapidly flickering/alternating stimuli have been extensively used for studies of the visual system. For example, individual neurons in the highly myelinated dorsal visual stream of primates have been shown to be able to follow stimuli alternating at rates up to 90 Hz (C. Gray, pers. commun.). However, most EEG/MEG studies have used stimuli presented at lesser rates, since neurons in visual cortical areas of the ventral stream are thought to follow frequencies not exceeding 25–30 Hz (see Fig. 2c; for review, see Ref. 2). For example, visual stimuli alternating at 4–28 Hz have been used in "steady state visual evoked potential" EEG/MEG experiments. Thus, for a current frequency alternating at ≈29 Hz the required repetition time of the ABSS pulse sequence needs to be TR = 17 ms,

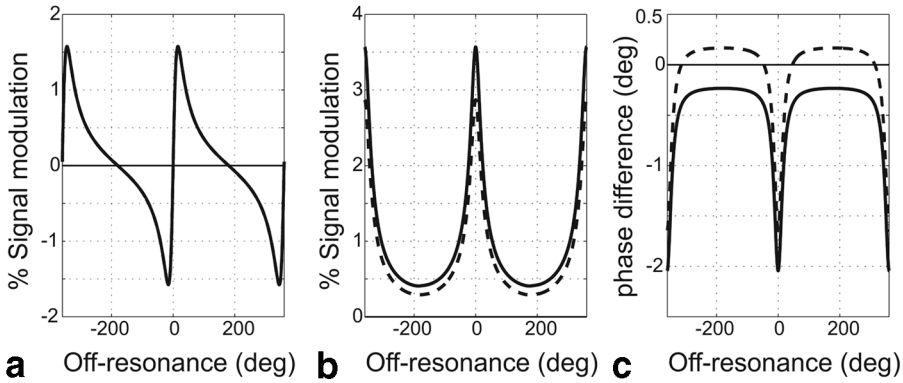

FIG. 4. Signal modulation between the two steady states. The difference of MR signal magnitudes in terms of percent nonmodulated signal magnitude (**a**), the magnitude of the complex difference in terms of percent nonmodulated magnitude (**b**), and the difference in signal phase (**c**) as a function of off-resonance. The continuous line: TE = 27 ms; broken line: TE = 3 ms. In **a** the two curves overlap. The current-induced free precession angle was alternating between $\Delta\phi = 0$ and $\Delta\phi = 0.5°$ (corresponding to $\Delta B_{\tilde{z}} \approx 1.1$nT). Simulation parameters are as for Fig. 3.

which sets a lower bound for the TR. The two bounds for the duration of ABSS TR results in the stimulation frequency range of 10–30 Hz (Fig. 2c).

MATERIALS AND METHODS

Computer simulations of the SSFP magnetization and MRI data analysis were performed using MatLab (MathWorks, Natick, MA). MRI images of a current phantom were acquired using a 3T GE Excite scanner (short bore) at the UCSD Center for fMRI and a GE receive/transmit knee quadrature coil. A 2D balanced SSFP sequence with a 1-shot spiral acquisition (±125 kHz) with flip angle = 27°, TE = 3 ms (spiral-out) and 27 ms (spiral-in), TR = 31 ms, FOV = 18 cm, 64 × 64 matrix and 4 mm slice thickness was used to acquire a single axial slice through the plane containing the wire inside a current phantom (see below). The RF pulse shape was a simple sinc pulse (bandwidth = 5 kHz), and the spiral trajectory was an Archimedean spiral that meets the minimum Fourier sampling criteria (30). A total of 600 images were acquired during experiments using 10–100 μA current and 1200 images were acquired for the weak currents, resulting in scan durations of 18 or 36 sec, respectively. Such short scan durations are determined by gradient hardware limitations and scanner drift (≈10 Hz drift over a period of a 5-min scan). The phase of the RF pulse was cycled using a 180° step. In order to explore the sensitivity of the bSSFP signal to static off-resonance, a static linear gradient (0.75 G/m) along the X axis was applied, which resulted in a characteristic periodic banding artifact. The magnitude of the modulation of the complex signal and the magnitude and phase fluctuations around the banding artifact of the signal were explored as a function of ΔB_z. The mean difference images were calculated by subtracting odd from even images and averaging 275 difference images (nreps = 550, initial 50 discarded to eliminate relaxation effects). Modulation of the complex MR signal by application of the periodic current was detected in each voxel using Hotteling's T_2 multivariate test (24). A voxel cluster was deemed modulated by current if Hotteling's T_2 test rejected the null hypothesis at $P < 0.05$ (uncorrected) in at least three adjacent voxels.

A spherical current phantom 100 mm in diameter filled with agar was used. The phantom recipe used $NiCl_2$ and an agar mixture such that T_1 and T_2 (100–110 ms) were comparable to gray matter; NaCl was added to increase the conductivity to mimic the RF load of a head (31). An insulated copper wire (≈0.6 mm in diameter) was placed in the middle of the phantom along the X-Y direction and perpendicular to the B_0 vector of the 3T scanner. Cables delivering current to the phantom were arranged parallel to the B_0 vector so that only the magnetic field created by current flowing in the perpendicular wire contributed to B_0. An ≈9 K° resistor was connected in series to the phantom wire. The current magnitude was controlled with synchronization precision of 20 μs via an analog output port of a National Instruments (Austin, TX) I/O card that received trigger TTL pulses from the scanner with every RF pulse. The card was programmed using LabView to set a desired temporal waveform locked to scanner RF pulses. The range of currents explored was 10 μA to 1 mA. ΔB_z in a given voxel was estimated by applying the Biot-Savart law to a long wire. The applicability of the Biot-Savart law was tested numerically by integrating the contribution of wire current segments to each voxel within a slice across the phantom that included the wire. For a long wire configuration in the vicinity of the wire the induced magnetic flux magnitude falls off as an inverse function of distance × from wire $B_z(x) = \mu_0 I/2\pi x$, where I is electric current, x is distance from the wire, and μ_0 is magnetic permeability of free space. For example, for I = 0.1 mA, B_z (20 mm) ≈ 1nT. We have verified this assumption by determining the decay of the ABSS signal modulation as a function of distance from the wire: The intensity of modulation by current indeed falls off inversely with the distance but may deviate somewhat from the inverse distance law due to spatial distortions of the modulation pattern caused by field inhomogeneities (see Results).

RESULTS

A typical pattern of current-induced fluctuations is shown in Fig. 5. The four top panels represent a) a typical ABSS image of the phantom, b) the magnitude of the mean complex difference between images corresponding to the two alternating steady states, c) the mean difference between the magnitude images of the two alternating steady states, and d) the mean difference in the phase images of the two states. Panels on the bottom row represent measured (filled circles) and theoretical (continuous lines) off-resonance profiles. The x axis (off-resonance) of the theoretical profiles is stretched to match that of the data.

The pattern of vertical stripes in the ABSS image (Fig. 5a) is a result of banding artifacts produced by application of the linear shim gradient along the X axis. The off-resonance offset between two adjacent minima of the bands is 1/TR ≈ 32 Hz. The banding artifact stripes are affected by the global inhomogeneity (imperfections in shimming) and also, next to the wire, by the magnetic field induced by the current, but the latter effect is weak and becomes negligible a few voxels away from the wire. A horizontal artifact in the middle of the phantom is caused by the susceptibility variations around the copper wire. The horizontal black line below the wire represents the location of the intensity profiles on the bottom row of Fig. 5. The dots represent measured voxel intensities and the continuous lines are theoretical solutions of the steady-state signal scaled to match the ABSS image intensity of Fig. 5a.

Images in Fig. 5b–d represent the modulation pattern caused by current alternating between 0 and ≈1 mA with every other RF pulse, according to the temporal pattern as in Fig. 1a. The current-induced ΔB_z at the distance indicated by the black line (≈20 mm below the wire) is ≈1nT. The image in Fig. 5b represents the magnitude of a complex difference between odd and even ABSS images, averaged over 275 repetitions. Note that the maximum signal modulation occurs not around transition bands (i.e., banding artifacts) but is centered on the middle of the "pass band" (high signal value), as predicted by the steady-state solution for ABSS (cf. Fig. 4). Filled circles with error bars in the panel below are modulation intensities and standard errors of the mean at voxels labeled in the image by

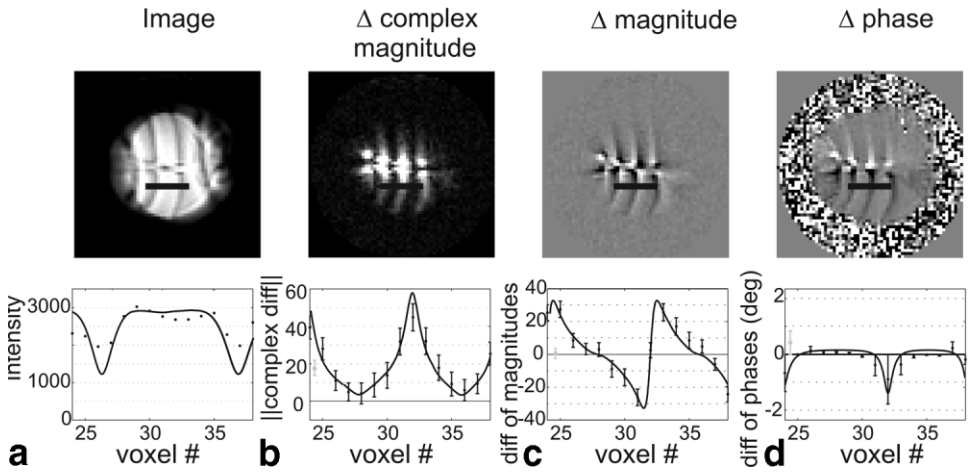

FIG. 5. ABSS images (top row) and intensity profiles (bottom row) 20 mm from the center (indicated by the black bar on the images). Top row: **a:** a typical ABSS magnitude image with an X linear shim gradient added (0.75 G/m); **b:** the mean magnitude of the complex difference between the two alternating states; **c:** the mean difference between magnitude images of the two states; **d:** the mean difference in phase. All difference images are averaged over 275 repeats. The continuous line in the bottom row graphs represents the theoretical intensity profiles and filled circles are the measured profiles. Error bars are standard errors of the mean. The y axis in the bottom **a–c** panels are in units of image intensity and the phase difference in the bottom **d** panel is in degrees. Scan parameters are: TR/TE = 31/27 ms, flip angle = 27°, scan duration 18 sec, FOV = 18 cm, matrix = 64 × 64, slice thickness = 4 mm, current = 100 μA. The gray point with error bars in **b–d** represents modulation in GRE experiments (TR/TE = 31/27 ms).

the black line. The continuous line is the theoretical prediction of the modulation profile given the image intensity scaling factor as in Fig. 5a. Note that the off-resonance profile is slightly different in shape from that presented in Fig. 4 since it is expressed in terms of the absolute modulation. The deviations of the data from the theoretical profile are due to partial voluming that results in smoothing of the off-resonance profile. When such smoothing is taken into account, the theoretical curve matches the data reasonably well despite the fact that no amplitude fitting was performed.

The mean difference between odd and even magnitude images acquired at ABSS (averaged over 275 pairs) is shown in Fig. 5c. The panel underneath plots the modulation profile across the black line of the top image. The continuous line is a theoretical prediction of a difference in off-resonance profiles of the two ABSS steady states. The overall shape accords well with the prediction (cf. dotted line in Fig. 5). The theoretical profile was calculated assuming only the intensity scaling factor for the image shown in Fig. 5a. The difference in phase images of the two ABSS steady states is shown in Fig. 5d. The bottom panel shows good agreement between the mean measured (dots with error bars representing standard error of the mean) and theoretical phase intensity profiles (continuous line).

The comparison of ABSS and GRE sensitivity to periodic ΔB_z perturbations is presented in Fig. 6. Figure 6a is a composite of two complex modulation images (time-averaged magnitude of the difference between complex images at the two steady states) acquired in experiments using alternating currents of ≈0.1 mA. The upper half shows a typical complex modulation pattern produced by ABSS imaging, while the lower half is produced using GRE imaging. The position of the wire corresponds to the white line dividing the two image halves. The black vertical line indicates the location used for modulation profiles of Fig. 6b,c.

Figure 6b plots the magnitude of the current-induced modulation of the complex signal as a function of the distance from the wire (as indicated by the black vertical line in Fig. 6a). The dots and error bars (indicating standard error of the mean) connected with a continuous black line represent the complex modulation in terms of percent mean image intensity acquired using ABSS (I = 100 μA, 18-sec scan, N = 275). The continuous black line is the best-fitting hyperbola (in terms of least squares) indicating that the magnitude of the complex modulation decays with the inverse of the distance from the wire carrying the current. The dots and error bars fitted by the broken line correspond to the magnitude of the complex modulation due to periodic current when the GRE sequence with TE = 27 ms was used (I = 100 μA, 18-sec scan, N = 275). The dots with error bars fitted by the dotted bar represents similar results when GRE with TE = 3 ms was used (I = 100 μA, 18-s scan, N = 275). Corresponding SNR values of all three scan protocols are plotted in Fig. 6c.

In the GRE experiments employing 100 μA alternating current (18-sec scan, N = 550), the modulation pattern was detectable using Hotteling's T_2 test (24) up to 15 mm away from the wire (the horizontal white broken line in the lower half of Fig. 6a), corresponding to the detection limit of $\Delta B_z \approx 1.5$ nT. By contrast, the ABSS signal was modulated according to the characteristic pattern and was reliably detectable up to the edge of the phantom (≈5 cm from the wire), corresponding to $\Delta B_z \approx 0.5$ nT.

We explored the limits of ABSS sensitivity to periodic currents by applying 10 and 20 μA currents to the phantom. Application of 10 μA alternating current in ABSS experiments resulted in detection (P = 0.05) of modulation in 33% of 18-sec scans (5 out of 15). In the five successful scans the mean detected minimum ΔB_z was 159 ± 82 pT.

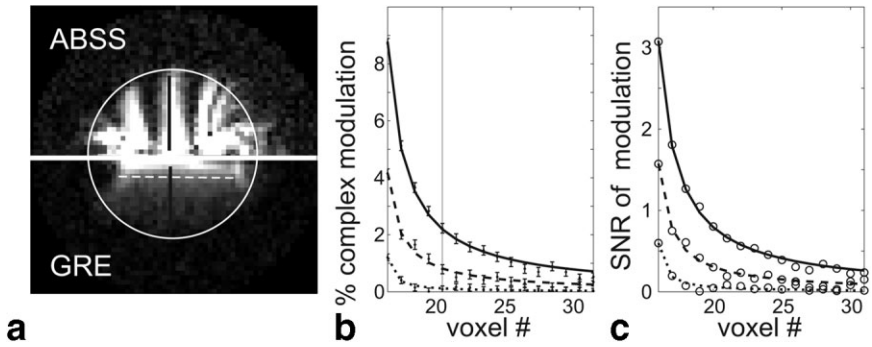

FIG. 6. Comparison of the current-induced signal modulation in ABSS and GRE experiments as a function of distance from the wire. **a:** Composite image of the average magnitude of the complex difference between the two alternating steady state images (top half) in the presence of an X-gradient (0.75 G/m) and GRE images corresponding to current-on vs. current-off intervals (bottom half); current amplitude = 100 μA; $n = 275$; acquisition time 18 sec. The white horizontal line separating the two half-images corresponds to the location of the wire. The two black vertical bars indicate pixels used for plotting profiles in **b** and **c**. **b:** The magnitude of complex modulation in terms of percent image magnitude as a function of the distance from the wire corresponding to the vertical black bar on the modulation image of panel **a**. The mean and standard error of the mean (dots with error bars) for the ABSS images (TR/TE = 31/27 ms) are fitted by the continuous line (the best-fitting hyperbola), for the GRE images acquired using long echo time are fitted by the broken line (TR/TE = 31/27 ms), and for the GRE images acquired using short echo time are fitted by the dotted line (TR/TE = 31/3 ms). The vertical line represents the cutoff distance at which modulation by current is detectable (1.5 nT). **c:** Temporal SNR of the complex modulation as a function of the distance from the wire, corresponding to the three scan protocols used for panel **b**.

In the experiment employing 20 μA current and a 36-sec scan ($N = 1150$), the modulation was detectable at the distance of ≈30 mm, corresponding to $\Delta B_z \approx 150$ pT, consistent with the 10 μA experiments.

DISCUSSION AND CONCLUSIONS

Our simulations and experiments on a phantom demonstrate that bSSFP imaging is highly sensitive to periodic alternating currents locked to RF pulses so that an alternating balanced steady state is reached. Succinctly, the advantage of the current imaging using ABSS as compared to GRE imaging is a result of two factors: the approximate ratio T_2/T_2^* of the effective phase accrual time for ABSS vs. GRE and the SNR_{ABSS}/SNR_{GRE} that further scales the signal. Indeed, our ABSS imaging experiments with a current phantom resulted in detection of magnetic field variations as small as ≈150 pT. Koon et al. (4) reported detection of magnetic field strength of 110 ± 50 pT using GRE imaging. In that study a scan duration of 62 min was required and the voxel volume was 144 mm^3. Bodurka and Bandettini (3) reported spin echo experiments that lead to detection of 200 pT perturbations lasting for 40 ms. In these experiments scan duration was 480 sec and voxel volume was 37.5 mm^3. ABSS imaging of periodic currents, by contrast, achieves comparable sensitivity in a mere 36 sec of scanning using 32 mm^3 voxels and 30 ms current pulses. Thus, the ABSS approach offers a substantial improvement in scan efficiency and hence in CNR of the current-modulated MR signal. Moreover, the parameters used herein for calculations of the ABSS signal sensitivity and the current experiments merely reflect our present scanner capabilities. The sensitivity of the ABSS signal to currents, as compared to that of GRE, can be improved by reducing TR and increasing flip angle (see Fig. 2). In vivo the actual improvement in sensitivity would be determined by the stimulus presentation frequency, distance to neuronal current dipoles and their orientation, as well as the contribution from physiological noise sources.

The ABSS-based imaging of electric currents is limited to detection of the periodic signal. Thus, application of ABSS to ncMRI would require utilization of periodic stimuli locked to RF pulses. The suitable stimulus frequency ranges between ≈10–30 Hz for experiments involving stimulus-evoked neuronal responses. Stimulus-evoked neuronal population responses can be easily synchronized by locking stimulus to the RF pulses. Since the neuronal response lags behind stimulus presentation with a latency of 50–100 ms in early visual cortex, EEG/MEG experiments may be instrumental in assessing optimal phase shift between the stimulus and RF pulses. An alternative is to acquire ncMRI data at several stimulus phase offsets since latencies vary broadly across cortical areas. Imaging of spontaneous cerebral rhythms by means of ABSS is technically challenging as it would require synchronization of RF pulses to these rhythms. In principle, in-scanner EEG could be used for such synchronization but it remains to be seen whether such an approach is feasible.

Even though the ABSS imaging of periodic currents affords a promising CNR, several obstacles need to be overcome before this method can be applied for imaging neuronal currents in vivo. First, the temporal variation in B_0 may compromise SSFP imaging, since it is highly sensitive to B_0 field variations. Periodic disturbances of B_0 due to the respiratory rhythm perturb the resonant frequencies, and thus steady-state response. The BOLD response can further perturb the resonant frequency due to the difference in resonant frequency of the deoxygenated and oxygenated hemoglobin. Main coil and gradient heating can impose an additional global gradual shift in resonant frequency. Lee et al. (32) proposed to compensate respiration-induced B_0 fluctuations and scanner drift in the bSSFP data by performing real-time measurements of the free induction decay (FID) phase. This novel respiration com-

pensation method is directly applicable to bSSFP-based imaging of neuronal currents.

Second, the sensitivity of bSSFP to an alternating ΔB_z stimulus depends on B_0 inhomogeneity with maximum sensitivity occurring around SSFP off-resonance zeros (assuming 180° phase cycling). In order to form images free of banding artifacts, imaging of weak neuronal currents using ABSS pulse sequences require careful higher-order shimming and placing of excitation frequency so that regions of interest fall in the interval of maximum sensitivity for ΔB_z modulation. In addition, application of multiple acquisitions using a range of phase cycling increments would be necessary for exhaustive artifact-free coverage of an imaging slice (33).

Third, the cardiac rhythm has been shown to be a major source of noise in ncMRI experiments employing EEG for detection of alpha waves by means of cross-coherence (13). These authors reported that pulsatile tissue motion associated with the systolic pressure wave in cerebral vasculature, as large as 300 μm in subcortical structures, contaminates EEG recordings and compromises detection of neuronal sources of alpha waves by means of GRE ncMRI. However, such noise sources in ABSS experiments are in a substantially lower frequency range compared to the rate of stimulation by induced neuronal currents and are not likely to be locked to the RF pulse train, and therefore would not contribute to the alternating steady states. A separate study is needed to address the impact on the ABSS signal of physiological noise sources and Poisson-like variability in neuronal response magnitudes and latencies.

Finally, our model for theoretical calculations and the current phantom experiments assume that the dominating source of MRI signal modulation is the mean ΔB_z variation in a voxel. Given this model, the ABSS imaging of weak currents has better sensitivity than other techniques and the experimental data support the theory. Further research is needed to determine if the pattern of ΔB_z offsets produced by neural currents is compatible with this model and whether it is detectable in vivo.

In conclusion, we show that ABSS imaging affords high sensitivity to periodic currents, but it remains to be seen whether the model assumptions employed herein are applicable for imaging of neuronal currents in vivo.

APPENDIX

Below we derive the steady-state magnetization for the ABSS pulse sequence using the propagation approach (27). In the interest of simplicity the echo time is assumed to be TE = TR/2. Given a phase-cycled (180°) RF pulse applied along the *x* axis through a tip angle $+\alpha$ for odd excitations and $-\alpha$ for even excitations, the nutation of a spin isochromat by RF pulses is represented by a rotation matrix $R_x(\pm\alpha)$. The current alternation is locked to excitation pulses (see Fig. 3). We assume that the current alternates such that the current-induced free precession angle is $\delta\phi_i$ rad and corresponds to an alternating off-resonance offset of $\delta f_i = \delta\phi_i/2\pi\tau$ Hz, where τ is precession time and i = 1,2 indexes the steady state (Fig. 3, bottom). Thus, the precession angle is different for odd and even TRs and is determined by off-resonance frequency Δf due to static magnetic field inhomogeneities and δf_i due to applied periodic current. Spin precession by an angle $\phi_i = 2\pi\tau(\Delta f + \delta f_i)$ between excitations is represented by a matrix $R_z(\phi)$ for rotation about the z axis.

Using matrix notation (27,34), the T_1 and T_2 relaxation can be represented by multiplying a magnetization vector M by $C(t) = \exp(-t/T)$, where $T = diag(T_2,T_2,T_1)$, and adding a vector $D(t) = (I - C(t))|0 \quad 0 \quad M_z|^T$. Here I is the 3×3 identity matrix and *diag* is a diagonal matrix. In the interest of simplicity, we derive magnetization at the time after the RF pulse τ = TE = TR/2 = TR-TE. Then the magnetization vectors M_q at the time points **q = b,c,d,e,f** with respect to those at the preceding labeled timepoint (see Fig. 4) are:

$$
\begin{aligned}
M_b &= R_z(\tau v_1)C(\tau)M_a + D(\tau),\\
M_c &= R_x(-\alpha)M_b,\\
M_d &= R_z(TRv_2)C(TR)M_c + D(TR),\\
M_e &= R_x(\alpha)M_d,\\
M_f &= R_z(\tau v_1)C(\tau)M_e + D(\tau),
\end{aligned}
\qquad [A1]
$$

where $v_i = 2\pi(\Delta f + \delta f_i)$ is the angular velocity of the free precession for the *i*-th steady state. Then during the $(k+1)$-th TR magnetization M_{k+1} is:

$$
\begin{aligned}
M_{k+1} = R_z(\tau v_1)C(\tau)R_x(\alpha)[R_z(TRv_2)C(TR)R_x(-\alpha)\\
\times [R_z(\tau v_1)C(\tau)M_k + D(\tau)] + D(TR)] + D(\tau).
\end{aligned}
$$

The steady state condition requires that magnetization recurs periodically $M_{k+1} = M_k$. This condition leads to a steady state solution of Eq. [A1] for the two alternating states as in Eq. [3] of the main text:

$$
\begin{aligned}
M_{SS1} &= (I - A_1)^{-1}B_1,\\
M_{SS2} &= (I - A_2)^{-1}B_2,
\end{aligned}
\qquad [A2]
$$

with

$$A_1 = E(\tau,v_1,\alpha)E(TR,v_2,-\alpha)C(\tau) \qquad [A2a]$$

$$B_1 = [E(\tau,v_1,\alpha)E(TR,v_2,-\alpha) + I]D(\tau) + E(\tau,v_1,\alpha)D(TR)$$

$$A_2 = E(\tau,v_2,-\alpha)E(TR,v_1,\alpha)C(\tau)$$

$$B_2 = [E(\tau,v_1,-\alpha)E(TR,v_1,\alpha) + I]D(\tau) + E(\tau,v_2,-\alpha)D(TR),$$

where $E(t,v,a) = R_z(tv)C(t)R_x(a)$. The propagation approach can be readily applied for derivation of the steady state magnetization vector $M(t)$ at an arbitrary time $t \in [0,TR]$.

ACKNOWLEDGMENTS

We thank Yousef Mazaheri, Geoffrey Boynton, Mirianas Chachisvilis, Jongho Lee, Karla Miller, and Martin Sereno

for insightful discussions, the anonymous referees for constructive suggestions, and Larry May and Cecelia Kemper for advice on manufacturing the phantom. Supported by Center for Functional MRI, Department of Radiology, UCSD.

REFERENCES

1. Ogawa S, Lee TM, Kay AR, Tank DW. Brain magnetic resonance imaging with contrast dependent on blood oxygenation. Proc Natl Acad Sci U S A 1990;87:9868–9872.
2. Nunez PL, Srinivasan R. Electric fields of the brain. Oxford: Oxford University Press; 2006.
3. Bodurka J, Bandettini PA. Toward direct mapping of neuronal activity: MRI detection of ultraweak, transient magnetic field changes. Magn Reson Med 2002;47:1052–1058.
4. Konn D, Gowland P, Botwell R. MRI detection of weak magnetic fields due to an extended current dipole in a conducting sphere: a model for direct detection of neuronal currents in the brain. Magn Reson Med 2003;50:40–49.
5. Bodurka J, Jesmanowics A, Hyde JS, Xu H, Estkowski L, Li SJ. Current-induced magnetic resonance phase imaging. J Magn Reson 1999;137: 265–271.
6. Yang H, Cook GG, Paley MN. Mapping of periodic waveforms using the ghost reconstructed alternating current estimation (GRACE) magnetic resonance imaging technique. Magn Reson Med 2003;50:633–637.
7. Chow LS, Cook GG, Whitby E, Paley MN. Investigation of MR signal modulation due to magnetic fields from neuronal currents in the adult human optic nerve and visual cortex. Magn Reson Imaging 2006;24: 681–691.
8. Chow LS, Cook GG, Whitby E, Paley MN. Investigating direct detection of axon firing in the adult human optic nerve using MRI. Neuroimage 2006;30:835–846.
9. Hatada T, Sekino M, Ueno S. Detection of weak magnetic fields induced by electrical currents with MRI: theoretical and practical limits of sensitivity. Magn Reson Med Sci 2004;3:159–163.
10. Petridou N, Plenz D, Silva AC, Loew M, Bodurka J, Bandettini PA. Direct magnetic resonance detection of neuronal electrical activity. Proc Natl Acad Sci U S A 2006;103:16015–16020.
11. Liston AD, Salek-Haddadi A, Kiebel SJ, Hamandi K, Turner R, Lemieux L. The MR detection of neuronal depolarization during 3-Hz spike-and-wave complexes in generalized epilepsy. Magn Reson Imaging 2004; 22:1441–1444.
12. Konn D, Leach S, Gowland P, Botwell R. Initial attempts at directly detecting alpha wave activity in the brain using MRI. Magn Reson Imaging 2004;22:1413–1427.
13. Mandelkow H, Halder P, Brandeis D, Soellinger M, de Zanche N, Luechinger R, Boesiger P. Heart beats the brain: the problem of detecting alpha waves by neuronal current imaging in joint EEG-MRI experiments. NeuroImage 2007;37:149–163.
14. Kamei H, Iramina K, Yoshikawa K, Ueno S. Neuronal current distribution imaging using magnetic resonance. IEEE Trans Magn 1999;35: 4109–4111.
15. Xiong J, Fox, PT, Gao, JH. Directly mapping magnetic field effects of neuronal activity by magnetic resonance imaging. Hum Brain Mapp 2003;20:41–49.
16. Chu R, de Zwart JA, van Gelderen P, Fukunaga M, Kellman P, Holroyd T, Duyn JH. Hunting for neuronal currents: absence of rapid MRI signal changes during visual-evoked response. NeuroImage 2004;23:1059–1067.
17. Bianciardi M, Di Russo F, Aprile T, Maraviglia B, Hagberg GE. Combination of BOLD-fMRI and VEP recordings for spin-echo MRI detection of primary magnetic effects caused by neuronal currents. Magn Reson Imaging 2004;22:1429–1440.
18. Hagberg GE, Bianciardi M, Maraviglia B. Challenges for detection of neuronal currents by MRI. Magn Reson Imaging 2006;24:483–493.
19. Bernstein MA, King KF, Zhou XJ. Handbook of MRI pulse sequences. Amsterdam: Elsevier; 2004.
20. Scheffler K, Lehnhardt S. Principles and applications of balanced SSFP techniques. Eur Radiol 2003;13:2409–2418.
21. Nayak KS Hargreaves BA, Hu BS, Nishimura DG, Pauly JM, Meyer CH. Spiral balanced steady-state free precession cardiac imaging. Magn Reson Med 2005;53:1468–1473.
22. Bieri O, Maderwald S, Ladd ME, Scheffler K. Balanced alternating steady-state elastography. Magn Reson Med 2006;55:233–241.
23. Overall WR, Conolly SM, Nishimura DG, Hu BS. Oscillating dual-equilibrium steady-state angiography. Magn Reson Med 2002;47:513–522.
24. Lee J, Shahram M, Schwartzman A, Pauly JM. Complex data analysis in high-resolution SSFP fMRI. Magn Reson Med 2007;57:905–917.
25. Gudbjartsson H, Patz S. Simultaneous calculation of flow and diffusion sensitivity in steady-state free precession imaging. Magn Reson Med 1995;34:567–579.
26. Zur Y, Stokar S, Bendel P. An analysis of fast imaging sequences with steady-state transverse magnetization refocusing. Magn Reson Med 1988;6:175–193.
27. Hargreaves BA, Vasanawala SS, Pauly JM, Nishimura DG. Characterization and reduction of the transient response in steady-state MR imaging. Magn Reson Med 2001;46:149–158.
28. Scheffler K, Hennig J. Is TrueFISP a gradient-echo or a spin-echo sequence? Magn Reson Med 2003;49:395–397.
29. Wansapura JP, Holland SK, Dunn RS, Ball WS. NMR relaxation times in the human brain at 3.0 Tesla. J Magn Reson Imag 1999;9:531–538.
30. Glover GH. Simple analytic spiral K-space algorithm. Magn Reson Med 1999;42:412–415.
31. Schneiders NJ. Solutions of two paramagnetic ions for use in nuclear magnetic resonance phantoms. Med Phys 1988;15:12–16.
32. Lee J, Santos JM, Conolly SM, Miller KL, Hargreaves BA, Pauly JM. Respiration-induced B0 field fluctuation compensation in balanced SSFP: real-time approach for transition-band SSFP fMRI. Magn Reson Med 2006;55:1197–1201.
33. Bangerter NK, Hargreaves BA, Vasanawala SS, Pauly JM, Gold GE, Nishimura DG. Analysis of multiple-acquisition SSFP. Magn Reson Med 2004;51:1038–1047.
34. Freeman R, Hill HDW. Phase and intensity anomalies in Fourier transform NMR. J Magn Reson 1971;4:366–383.